Gas-Induced Segregation in Pt-Rh Alloy Nanoparticles Observed by In Situ Bragg Coherent Diffraction Imaging

Tomoya Kawaguchi, Thomas F. Keller, Henning Runge, Luca Gelisio, Christoph Seitz, Young Yong Kim, Evan R. Maxey, Wonsuk Cha, Andrew Ulvestad, Stephan O. Hruszkewycz, Ross Harder, Ivan A. Vartanyants, Andreas Stierle, and Hoydoo You

Phys. Rev. Lett. **123**, 246001 — Published 13 December 2019

DOI: 10.1103/PhysRevLett.123.246001

Gas-induced segregation in Pt-Rh alloy nanoparticles observed by *in-situ* Bragg coherent diffraction imaging

Tomoya Kawaguchi,[1,6,] Thomas F. Keller,[2,3] Henning Runge,[2,3] Luca Gelisio,[2] Christoph Seitz,[2]
Young Y. Kim,[2] Evan R. Maxey,[4] Wonsuk Cha,[4] Andrew Ulvestad,[1,§] Stephan O. Hruszkewycz,[1] Ross Harder,[4]
Ivan A. Vartanyants,[2,5] Andreas Stierle[2,3] and Hoydoo You[1,*]

[1]*Materials Science Division, Argonne National Laboratory, Argonne, Illinois 60439, USA*

[2]*Deutsches Elektronen-Synchrotron DESY, D-22603 Hamburg, Germany*

[3]*Physics Department, Universität Hamburg, D-20355 Hamburg, Germany*

[4]*Advanced Photon Source, Argonne National Laboratory, Argonne, Illinois 60439, USA*

[5]*National Research Nuclear University MEPhI, 115409 Moscow, Russia*

[6]*Institute for Materials Research, Tohoku University, Sendai, 9808577, Japan*

[§] *Current Address: Tesla, Inc.*

[*] *hyou@anl.gov*

Bimetallic catalysts can undergo segregation or redistribution of the metals driven by oxidizing and reducing environments. Bragg coherent diffraction imaging (BCDI) was used to relate displacement fields to compositional distributions in crystalline Pt-Rh alloy nanoparticles. 3D images of internal composition showed that the radial distribution of compositions reverses partially between the surface shell and the core when gas flow changes between O_2 and H_2. Our observation suggests that the elemental segregation of nanoparticle catalysts should be highly active during heterogeneous catalysis and can be a controlling factor in synthesis of electrocatalysts. In addition, our study exemplifies applications of BCDI for *in situ* 3D imaging of internal equilibrium compositions in other bimetallic alloy nanoparticles.

Transition metals and their metal alloys have been extensively studied as materials for heterogeneous catalysis and electrocatalysis. In particular, metals in the platinum group and their alloys are among the most important catalysts for organic and electrochemical reactions [1,2]. In industrial applications, they are typically used as nanoparticles to increase efficiency and selectivity. For this reason, the size-shape-activity relationships have been a focus of extensive studies and the importance of surface reactions has been recognized [3,4]. In some studies, it was further suggested that the shapes and sizes of the nanoparticles can change during reactions. For example, the surface compositions of bimetallic nanoparticles were reported to change depending on oxidizing or reducing environments[5,6]. Since the changes occur during reactions, studies must be carried out *in-situ* in detail on an individual nanoparticle to fully understand the internal dynamics of elemental distributions.

A Pt-Rh alloy nanoparticle is an excellent system to study the effect of surface reactions on the compositional redistributions. The unit cell structures of both Pt and Rh are face-centered cubic (fcc) with 3% differences in lattice constants (a_{Pt}=3.9242 Å, a_{Rh}=3.8034 Å). In bulk, they form solid solutions with no phase separation [7] and negligible compositional ordering[8]. Since there are no significant internal driving forces for compositional redistribution, external driving forces by surface reactions can have a significant effect. If the effect of the surface reactions can be detected in a particle with a diameter of ~100 nm, which is roughly the size needed in this study for a suitable signal-to-noise ratio, we expect that the effect must be significant and relevant for real catalyst nanoparticles with higher surface-to-volume ratios.

Bragg coherent diffraction imaging (BCDI) is increasingly popular for imaging single-crystal nanoparticles under *in-situ* conditions [9-11]. The 3D real-space images reconstructed using BCDI are composed of voxels of complex numbers. The amplitude of the voxel is in principle proportional to the electron density of the crystalline order [12,13], while the phase is to the displacement of the crystallographic planes [14-16]. However, the degree of crystalline order within the particle is generally unknown and the amplitude alone can be unreliable in measuring electron densities. On the other hand, the *phase* of a BCDI image is sensitive to lattice displacements. The phase can also in principle be affected by the refraction effect [17] and the dynamical scattering effect [18]. However, because the nanoparticle size in our measurements is small compared to the extinction length or the Pendellösung length, the dynamical effects are small and the phase is dominantly proportional to the lattice displacement [18]. Therefore, use of the phase image guided by the amplitude image can provide the reliable composition distribution of a binary alloy nanoparticle by relating the lattice spacings to the local compositions.

The lattice spacing can be obtained from the atomic displacement field, $u_{111}(\boldsymbol{r})$, of the phase image reconstructed in BCDI. First, the lattice spacing deviation from the average is obtained from the derivative of the longitudinal displacement, $\partial_{111} u_{111}(\boldsymbol{r})/\partial r_{111}$ [16,19]. In the case of electrochemical dealloying [19], the deviation was used to map the *mechanical* strain at room temperature induced by the dealloying process. In the case of an alloy nanoparticle at high temperatures, however, the alloy elements can diffuse freely and the mechanical strain can be replaced by the *compositional strain*, i.e., the strain induced by the compositional heterogeneity [20-25]. Then, the local composition can be determined from the compositional strain via Vegard's law assuming that the changes in local composition isotopically expand/contract the cubic unit cell [26]. Thus, we will present our results as 3D images of local Rh compositions converted from the phase [20] and 3D images of normalized electron densities.

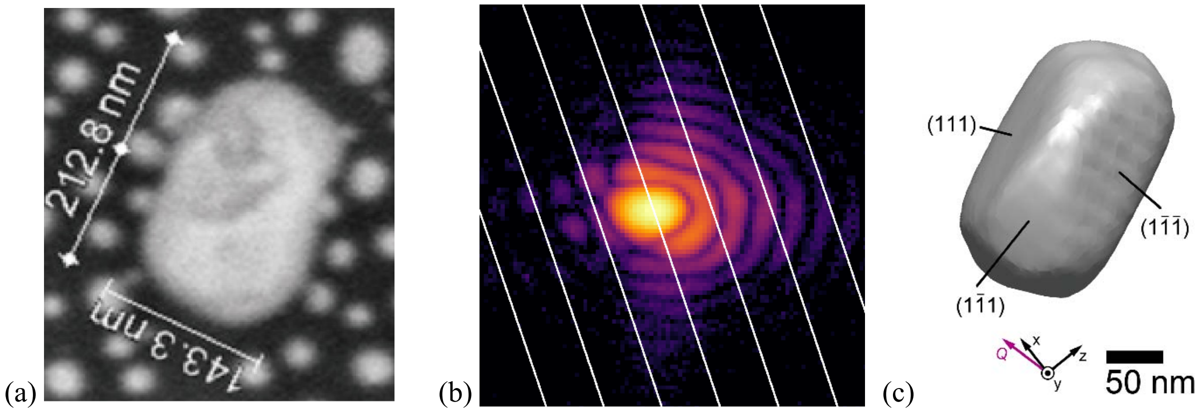

Fig. 1. (a) An SEM image of the Pt$_{2/3}$-Rh$_{1/3}$ alloy nanoparticle obtained after the BCDI measurements. The smaller nanoparticles in the SEM image are Rh particles. (b) A 2D coherent diffraction pattern of the 111 peak from the particle in a logarithmic intensity scale. The white equi-2θ lines indicate the expected Bragg peak maximum for every 10% change in the mean Rh composition of the particle. (c) A 3D reconstruction of the same particle using BCDI in a top-down view as is in (a). Isosurface of 45% of the mean electron density is drawn. *x, y,* and *z* of the laboratory coordinate system correspond to the radial direction of the synchrotron ring, the vertical direction, and the incident x-ray direction, respectively. The slightly larger size and the smoother shape of (c) compared with (a) are due the BCDI resolution lower than that of SEM.

Fig. 1 shows a scanning electron microscopy (SEM) image of the sample nanoparticle with a nominal $Pt_{2/3}$-$Rh_{1/3}$ composition (a), a slice of the Bragg diffraction data from the particle (b), and a 3D shape reconstructed from the data (c). The sample was prepared by depositing a Rh layer at 630 ºC over Pt nanoparticles dewetted on Al_2O_3(0001) substrate. Among several particles examined and tested [20], the nanoparticle shown in Fig. 1(a) was selected for detailed studies. Hierarchical fiducial markers were used to identify the same particle with an SEM and with a confocal microscope in the beamline. The 3D shape (c) and 3D phase were reconstructed by iterative phase retrieval algorithms standard for BCDI [27,28] in combination with a guided genetic algorithm [29] after applying flat-field correction on the detector and subtracting background scattering. The voxel size of BCDI images was ~6.7 nm and the resolution was ~13 nm [20]. The diffraction pattern did not change over the long x-ray exposure indicating that x-ray-induced oxidations were negligible, which is consistent with prior observations on the novel metals [30].

The sample temperature was independently estimated from the Al_2O_3 (0006) substrate peak position at each setting temperature based on the thermal expansion known in the literature [31]. Then, the average composition of the sample nanoparticle at that temperature was determined from the Bragg scattering angle of the nanoparticle from the known thermal expansion rates of the Pt-Rh alloys in the literatures [32,33]. This provided us a means of determining the particle average composition precisely for any given environment and temperature. The initial average composition at 550 °C determined in this way was close to our target composition of $Pt_{2/3}Rh_{1/3}$ although the composition evolved continuously depending on the environment and temperature during the course of the experiments [20].

The BCDI measurements were carried out under variable gas environments at atmospheric pressures, (i) pure He, (ii) He with 2.7%O_2, (iii) He with 5%O_2, and (iv) He with 3.8%H_2, at two temperatures, 550 and 700 °C.The environments were chosen for (i) neutral, (ii) (iii) oxidizing, and (iv) reducing conditions and the two temperatures were chosen for different Rh diffusion lengths. Rhodium atoms in a Pt matrix are expected to diffuse 6 nm and 70 nm at these temperatures, respectively [34,35], over the diffusion time of 10^3 sec, which is close to the approximate wait time at each gas change. The diffusion length at 550 °C was not sufficient to achieve a full thermal equilibrium over the entire particle but was sufficient for composition redistributions to be seen in BCDI measurements. At the elevated temperature of 700 °C, the particle-average lattice spacing decreased significantly over time [20], indicating the alloy nanoparticles slowly incorporated Rh atoms from neighboring Rh nanoislands during the experiment. The Rh incorporation was not significant at 550 °C but the lattice spacing responded whenever the gas flows were changed. The measurements at 400 °C or below showed little effect of gas environments [20] as expected from the extremely short thermal diffusion lengths of 0.15 nm for 10^3 sec diffusion.

Fig. 2 shows the 3D images of normalized amplitude (a) and composition difference (b) reconstructed at 550 °C. The H_2 exposure significantly decreased the electron density of the particle as indicated by the irregularities in the isosurfaces shown in Fig. 2(a), while the exposures of He and O_2 have almost no effect on the particle shape. While the density irregularity suggests an increased Rh composition, it can also indicate a significant reduction in crystalline order [12,13] as discussed earlier. Hence, the composition images obtained from the phase [20] are shown in Fig. 2(b) as the cross-sectional views of the Rh-composition variations. In an oxidizing atmosphere (O_2), only subtle growth of the Pt-rich region (green region) was observed near the surface. A reducing atmosphere (H_2), however, significantly affected the diffraction patterns [20] and the composition accordingly, as Rh-rich regions (purple region) formed and composition variations within the particle became significant.

The particle shape obtained from the BCDI remained largely unchanged at 700 °C and electron density isosurfaces in Fig. 2(c) appeared not sensitive to gas environments. However, upon a close inspection of the images in Fig. 2(c), some shape change can be seen in the H_2 atmosphere at the initial 5 min exposure of 3.8%H_2. The shape was restored in the images for the 30 and 76 min exposures, presumably as the system reached a steady state or a full thermal equilibrium because of the faster diffusion of Rh at this temperature. The compositions, shown in Fig. 2(d), indicate a significant Rh segregation near the surface in all gas environments.

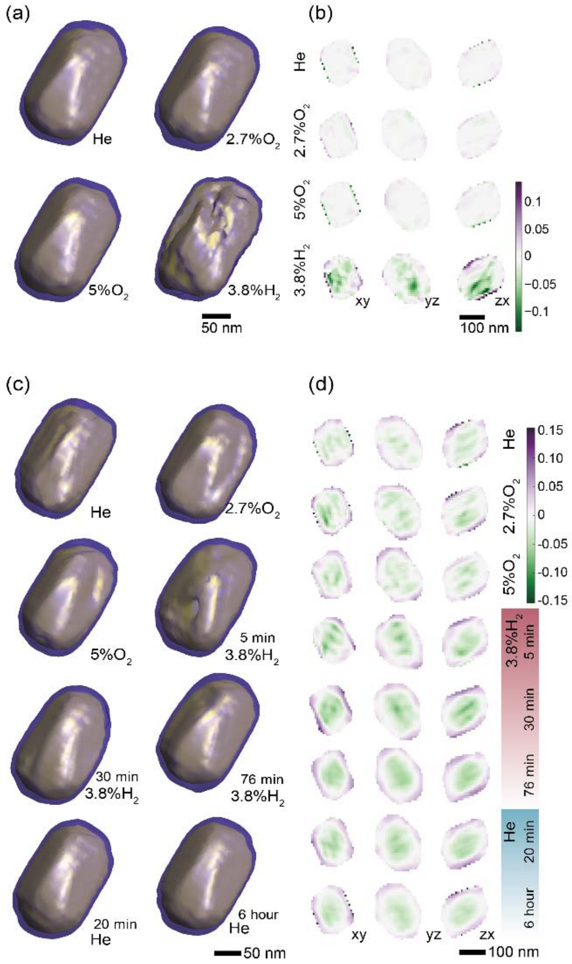

Fig. 2. (a,c) Electron density normalized by the maximum amplitude and (b,d) Rh composition difference from the particle average, obtained from compositional strain at various gas atmospheres at 550 °C (a,b) and at 700 °C (c,d). (a,c) Translucent isosurfaces at 45% (blue envelope), and 85% (yellow core) of the mean electron density are shown. See the supplementary movies files for 3D renderings with the 45% and 85% isosurfaces. (b,d) The color bar indicates the Rh composition difference ($\boldsymbol{\Delta x_{\mathrm{Rh}} = x_{\mathrm{Rh}} - \bar{x}_{\mathrm{Rh}}}$)[20] where $\boldsymbol{\bar{x}_{\mathrm{Rh}} \simeq 0.33}$ and x_{Rh} ranges from ~0.13 (green) to ~0.48 (purple) depending on the exact value of the particle average, $\boldsymbol{\bar{x}_{\mathrm{Rh}}}$.

The phase images were further analyzed to obtain the radial distributions of the composition. The radial distributions in Fig. 3 were calculated as a function of the distance from the 45% isosurface defined in Fig. 2. The radial distance of a voxel was defined as the distance *from* the nearest voxel on the 45% isosurface. Then, the radial distance up to 60 nm measured from the surface was divided to 25 shells and the Rh compositions were averaged at each shell. The number of the voxels was typically ~700 at the surface compared to ~30 at the core of the particle [20]. The errors in the radial distribution were estimated from the variance of the averaged values and the number of the voxels. The zero of the Rh composition (y axis) was set to the compositions averaged for the core of the particle, defined by the radial distance from the surface larger than 40 nm, to show clearly the differences at the surface.

In Fig. 3(a), the radial distribution for the 550 °C images clearly demonstrates the sensitivity of the surface composition to the gas environments. In 5%O_2 environment, the Pt-rich (Rh-poor) region appeared at the bins near the surface (< 15 nm) while the composition is relatively flat in He and in 2.7%O_2. At the same time, the average Rh composition (inset) decreased slightly under 2.7%O_2 atmosphere, which continued under 5% O_2. The decrease of the average Rh composition continues (inset) and Rh composition depletes further near the surface (◊). On the other hand, the H_2 atmosphere yields the 6% *increase* of Rh-composition due to Rh segregation at the surface as well as the considerable increase of the average Rh composition. The relatively large error bars and the step in the composition around 30 nm are due to the compositional fluctuation inside the particle as seen in Fig. 2(b). Averaging the Rh distribution in the 30 nm shell is not as smooth as the surface shells because the only small number of voxels were averaged while there are still significant compositional fluctuations.

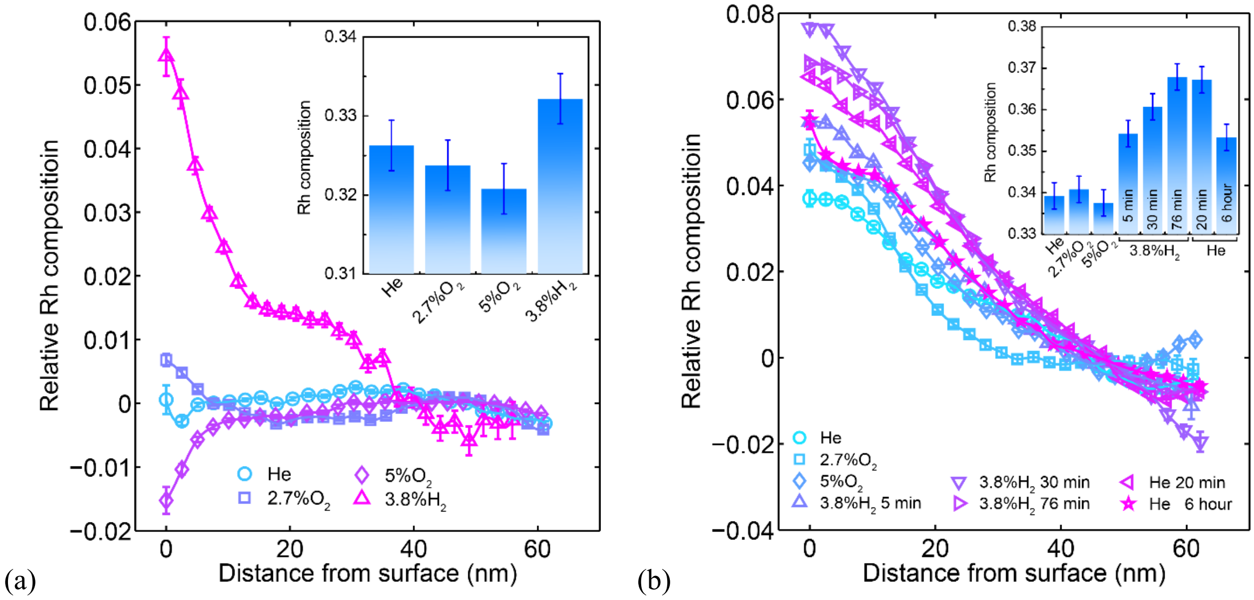

Fig. 3. Radial distributions of the relative Rh composition converted from compositional strain at 550 °C (a) and (b) at 700 °C. The zeros of the relative Rh compositions were set to the mean values of the compositions in the core of 40 nm or larger from the surface. The displayed times in (b) are the elapsed times after the gas introductions. The insets exhibit the particle average compositions of Rh determined from the Bragg angles. These values are used to set the zeros in the vertical scale bars in Fig. 2. Error bars in the inset was estimated from the pixel size of the 2D detector.

In Fig. 3(b) at 700 °C, the increased Rh compositions near the surface are evident regardless of the gas environments, even under O_2 flow. However, the trend of the Rh surface further segregation in H_2 (Δ, ▯,▯) was still consistent with the results at 550 °C. The increased Rh composition at the surface also led to a steady increase of the overall Rh composition as shown in the inset. When the gas was switched back to He (◃ and ☆), however, the Rh-rich surface region and the overall Rh composition decreased back slowly with time. In He flow, the composition slope decreased but still remained even after 6 hours.

Our results show that compositional distribution of Pt-Rh alloy nanoparticles is dynamic at high temperatures and sensitive to the environment condition. Some rationale to the observed behavior is illustrated in Fig. 4. Since the sample was exposed to air after preparation, the particle surface was initially covered by native oxides of rhodium because rhodium can form crystalline oxides such as hexagonal Rh_2O_3 or rutile RhO_2 while platinum does not easily form crystalline oxides [36]. The native oxides are expected to be extremely thin, limited to a few atomic layers, as illustrated in Fig. 4(a) since the sample is cooled to room temperature before exposure to air. Note that any diffraction from the oxides, thin or thick, unlikely contribute to the 111 Bragg peak measured here because of its different crystalline structure. Nonetheless, Rh oxide formation is expected and can be a driving force for the observed compositional redistribution in oxidizing environments [6,37].

When the particle is heated in the O_2 atmosphere, Rh, being more oxophilic than Pt, [38] forms oxides faster and thicker than Pt does. This causes Rh dealloyed at the surface of the particle by forming Rh oxides, which eventually yields the Rh-poor, Pt-rich region on the surface as in Fig. 4(b). In the H_2 atmosphere, the reverse reaction is expected. The Rh oxide is reduced and Rh atoms are incorporated to the particle. This simple oxidation-reduction model does not completely explain the results that the Rh was significantly enriched in the H_2 atmosphere. If the Rh oxides formed in O_2 simply incorporated back to the particle in H_2, the Rh composition on the surface could not have increased as significantly as observed.

The composition increase of Rh at the surface was 0.06, as shown in Fig. 3(a). The actual surface composition profile can be much narrower and higher because the distribution is a convolution of the actual distribution with the BCDI resolution (13 nm). Such significant surface segregation can occur only if external Rh atoms, diffused from neighboring Rh nanoislands, are incorporated to the surface of the particle. Although we have no direct evidence, it is likely even at 550 ºC that Rh atoms shuttle back and forth from the neighboring Rh nanoislands surrounding the Pt-Rh particle of this study. The Rh migration explains naturally the Rh-rich surface. This also increases the overall Rh composition as illustrated in Fig. 4 (c), which could not have taken place without the Rh migration.

At the relatively high temperature of 700 °C, the situation may be different. The equilibrium oxygen partial pressure of the Rh oxidation is quite high at $\sim 10^{-2}$ atm [38], which means that Rh oxides tend to spontaneously reduce to metal in the He atmosphere. Thus, alloying Rh by the Rh migration can continue at this temperature without the Rh oxide on the surface in He atmosphere as well as in H_2 atmosphere. As discussed earlier, the diffusion length of Rh at this temperature is 70 nm at 10^3 sec that is as large as the average radius of the particle, allowing the entire particle to reach a full thermodynamic equilibrium whenever the gas environment is changed. This explains why the radial distributions appear all similar in the different gases. However, it still shows significant changes of the Rh composition near the surface depending on the gas flow, much like the case at 550 °C. The continuous Rh migration from the Rh nanoislands explains the overall slope of the gradual decrease of Rh from the surface to the core.

However, it is also possibly driven thermodynamically towards the truncated surface [3] as experimentally observed in Rh-Pt nanoparticles [39], which requires further theoretical clarification.

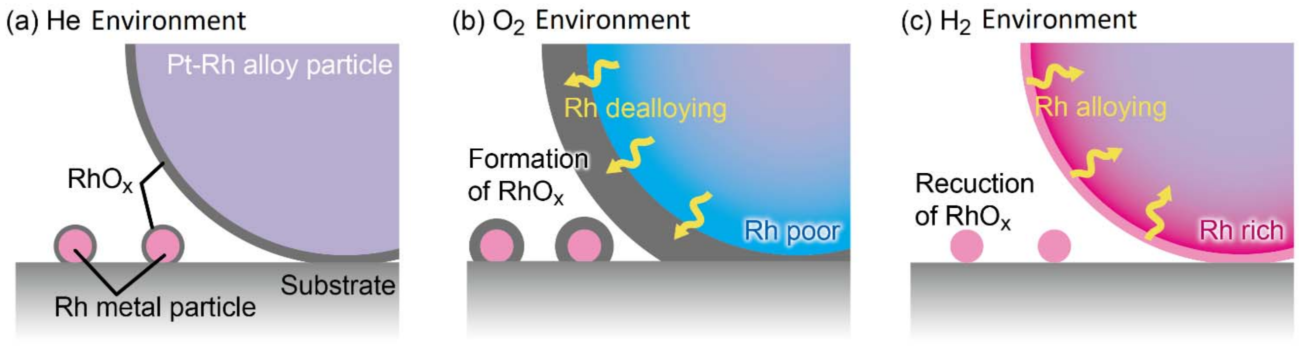

Fig. 4. Schematics of alloying and dealloying processes in He, O_2, and H_2 environments. (a) In He, the surfaces of the Pt-Rh particle and Rh nanoparticles all have a thin native oxide layer. (b) In O_2, Rh oxide layer grow faster because Rh is more oxophilic than Pt. (c) In H_2, the Rh oxide layer reduces, which increases the Rh compositions at the surface.

In conclusion, the BCDI technique, highly sensitive to nanoscale variations of lattice constants, is shown to be a powerful technique in studying *in situ* 3D internal composition map and dynamic shell-core compositional rearrangement in a $Pt_{2/3}$-$Rh_{1/3}$ alloy nanoparticle. At the intermediate temperature of 550 ºC, the surface Rh composition significantly decreases in an oxidizing environment and increases in a reducing environment. At higher temperatures, the Rh composition is significantly higher on the surface regions and gradually decreases towards the core of the particle regardless of the gas environments. However, the composition distribution shows the gas dependences similar to the results at 550 ºC. The redistributions of metals observed in alloy nanoparticles as large as ~100 nm offers an insight into the dynamic nature of the generally much smaller nanoparticle catalysts in practical usages, in particular for gas-phase catalysis and in fuel-cell catalysts operating at elevated temperatures, suggesting that the active compositional segregation, redistribution and other structural dynamics must be taken into account for rational design of new catalysts and electrocatalysts. This study also open a possibility of composition imaging studies on other binary alloys in equilibrium under various extreme environmental conditions.

Acknowledgements

Bragg coherent diffraction imaging x-ray measurements and data analysis was supported by the U.S. Department of Energy, Office of Science, Basic Energy Sciences, Materials Sciences Engineering Division. Use of the Advanced Photon Source was supported by the U.S. Department of Energy, Office of Science, Office of Basic Energy Sciences, under Contract No. DE-AC02-06CH11357. The work at DESY, x-ray measurements, sample preparation, and marker-based nano-transfer, was supported by the EU-H2020 research and innovation program under grant agreement No 654360 NFFA-Europe (TFK HG CS AS) and the Helmholtz Associations Initiative and Networking Fund and the Russian Science Foundation, grant number HRSF-0002 (LG YYK IAV). The use of the FIB dual beam instrument granted by BMBF (5K13WC3, PT-DESY) is acknowledged. We thank S. Kulkarni and A. Jeromin (DESY NanoLab [21]) for marking the regions of interest by IBID/EBID and the SEM post-analysis . One of the authors (TK) thanks the Japanese Society for the Promotion of Science (JSPS) for JSPS Postdoctoral Fellowships for Research Abroad.

Reference

[1] G. A. Somorjai and Y. Li, *Introduction to surface chemistry and catalysis* (Wiley, Hoboken, N.J., 2010), 2nd edn.

[2] G. Ertl, *Reactions at Solid Surfaces* (Wiley, 2009).

[3] C. Burda, X. B. Chen, R. Narayanan, and M. A. El-Sayed, Chemical Reviews **105**, 1025 (2005).

[4] V. Komanicky, H. Iddir, K.-C. Chang, A. Menzel, G. Karapetrov, D. Hennessy, P. Zapol, and H. You, Journal of the American Chemical Society **131**, 5732 (2009).

[5] F. Tao *et al.*, Science **322**, 932 (2008).

[6] P. Müller, U. Hejral, U. Rütt, and A. Stierle, Phys. Chem. Chem. Phys. **16**, 13866 (2014).

[7] S. B. Maisel, T. C. Kerscher, and S. Müller, Acta Materialia **60**, 1093 (2012).

[8] C. Steiner, B. Schönfeld, M. J. Portmann, M. Kompatscher, G. Kostorz, A. Mazuelas, T. Metzger, J. Kohlbrecher, and B. Demé, Physical Review B **71**, 104204 (2005).

[9] M. A. Pfeifer, G. J. Williams, I. A. Vartanyants, R. Harder, and I. K. Robinson, Nature **442**, 63 (2006).

[10] I. Robinson and R. Harder, Nature materials **8**, 291 (2009).

[11] M. e. a. Abuin, ACS Appl. Nano Mater. **2**, 4818 (2019).

[12] A. Ulvestad, J. N. Clark, R. Harder, I. K. Robinson, and O. G. Shpyrko, Nano Letters **15**, 4066 (2015).

[13] X. P. Liu, M. A. G. Aranda, B. Chen, P. M. Wang, R. Harder, and I. Robinson, Crystal Growth & Design **15**, 3087 (2015).

[14] W. Cha, S. Song, N. C. Jeong, R. Harder, K. B. Yoon, I. K. Robinson, and H. Kim, New Journal of Physics **12**, 035022 (2010).

[15] W. Cha *et al.*, Nature Materials **12**, 729 (2013).

[16] I. A. Vartanyants and I. K. Robinson, Journal of Physics-Condensed Matter **13**, 10593 (2001).

[17] R. Harder, M. A. Pfeifer, G. J. Williams, I. A. Vartaniants, and I. K. Robinson, Physical Review B **76**, 115425 (2007).

[18] W. Hu, X. J. Huang, and H. F. Yan, Journal of Applied Crystallography **51**, 167 (2018).

[19] W. Cha, Y. Liu, H. You, G. B. Stephenson, and A. Ulvestad, Advanced Functional Materials **27**, 1700331 (2017).

[20] See Supplementary Material for experimental and data analysis details includes Refs. [21-25]

[21] A. Stierle, T. F. Keller, H. Noei, V. Vonk, and R. Roehlsberger, J. Large-Scale Res. Facil. **2**, A76 (2016).

[22] H. N. Chapman *et al.*, Journal of the Optical Society of America a-Optics Image Science and Vision **23**, 1179 (2006).

[23] T. Kimura *et al.*, Nature Communications **5**, 3052 (2014).

[24] A. Ulvestad, A. Singer, J. N. Clark, H. M. Cho, J. W. Kim, R. Harder, J. Maser, Y. S. Meng, and O. G. Shpyrko, Science (New York, N.Y.) **348**, 1344 (2015).

[25] D. Shapiro *et al.*, Proceedings of the National Academy of Sciences of the United States of America **102**, 15343 (2005).

[26] T. Kawaguchi, W. Cha, V. Latyshev, S. Vorobiov, V. Komanicky, and H. You, Journal of the Korean Physical Society **75**, 528 (2019).

[27] W. Yang, X. Huang, R. Harder, J. N. Clark, I. K. Robinson, and H.-k. Mao, Nature Communications **4**, 1680 (2013).

[28] J. N. Clark, X. Huang, R. Harder, and I. K. Robinson, Nature Communications **3**, 993 (2012).

[29] C.-c. Chen, J. Miao, C. W. Wang, and T. K. Lee, Physical Review B **76**, 064113 (2007).

[30] V. Komanicky, D. C. Hennessy, H. Iddir, P. Zapol, and H. You, Electrochimica Acta **109**, 440 (2013).

[31] W. M. Yim and R. J. Paff, Journal of Applied Physics **45**, 1456 (1974).

[32] B. J. W. Arblaster, Platinum Metals Review, 184 (1997).

[33] J. W. Arblaster, Platinum Metals Review **41**, 12 (1997).

[34] T. Li, P. A. J. Bagot, E. A. Marquis, S. C. E. Tsang, and G. D. W. Smith, Catalysis Today **116**, 4760 (2012).

[35] P. Shewmon, *Diffusion in Solids* (Wiley, 1989), Second Edi edn.

[36] O. Muller and R. Rustum, J. Less-Common Metals **16**, 129 (1968).

[37] U. Hejral, D. Franz, S. Volkov, S. Francoual, J. Strempfer, and A. Stierle, Physical Review Letters **120**, 126101 (2018).

[38] T. B. Reed, *Free Energy of Formation of Binary Compounds* (MIT Press, Cambridge, 1971).

[39] Z. Wang, J. Ansermet, C. P. Slichter, and J. H. Sinfelt, J. Chem. Soc. Faraday Trans. 1 **84**, 3785 (1988).